

# *A clear link connecting the troposphere and ionosphere: ionospheric responses to the 2015 Typhoon Dujuan*

**Jian Kong, Yibin Yao, Yahui Xu,  
Chungyen Kuo, Liang Zhang, Lei Liu &  
Changzhi Zhai**

## **Journal of Geodesy**

Continuation of Bulletin Géodésique  
and manuscripta geodaetica

ISSN 0949-7714

Volume 91

Number 9

J Geod (2017) 91:1087-1097

DOI 10.1007/s00190-017-1011-4



**Your article is protected by copyright and all rights are held exclusively by Springer-Verlag Berlin Heidelberg. This e-offprint is for personal use only and shall not be self-archived in electronic repositories. If you wish to self-archive your article, please use the accepted manuscript version for posting on your own website. You may further deposit the accepted manuscript version in any repository, provided it is only made publicly available 12 months after official publication or later and provided acknowledgement is given to the original source of publication and a link is inserted to the published article on Springer's website. The link must be accompanied by the following text: "The final publication is available at [link.springer.com](http://link.springer.com)".**

# A clear link connecting the troposphere and ionosphere: ionospheric responses to the 2015 Typhoon Dujuan

Jian Kong<sup>1</sup> · Yibin Yao<sup>2</sup> · Yahui Xu<sup>2</sup> · Chungyen Kuo<sup>3</sup> ·  
 Liang Zhang<sup>2</sup> · Lei Liu<sup>2</sup> · Changzhi Zhai<sup>2</sup>

Received: 10 August 2016 / Accepted: 22 February 2017 / Published online: 4 March 2017  
 © Springer-Verlag Berlin Heidelberg 2017

**Abstract** The global navigation satellite system (GNSS) total electron content (TEC) sequences were used to capture the arrival time and location of the ionosphere disturbances in response to the 2015 Typhoon Dujuan. After removing the de-trended TEC variation, the clear ionosphere disturbances on the typhoon landing day could be distinguished, and these disturbances disappeared from the TEC sequences before and after the typhoon landing day. The foF2 data observed by Xiamen ionosonde station also show ionosphere disturbances. Based on the advantages of GNSS multi-point observations, the disturbances horizontal velocity in the ionosphere were estimated according to the linear theory for a dispersion relation of acoustic gravity waves (AGWs) in an isothermal atmosphere. The average horizontal velocity (~240 m/s) and the radial velocity (~287 m/s) were used in the two-dimensional grid search for the origin point on the Earth's surface. The origin area was determined to be on the eastern side of Taiwan. Lastly, a possible physical mechanism is discussed in this study. When typhoons land on Taiwan, the severe convective storms and the drag effect from the Central Mountains create an ideal location for development of AGWs. Topographic conditions, like the high lapse rate, contribute to the formation of AGWs, which then propagates into the ionosphere altitude.

**Keywords** GNSS TEC · Typhoon · Ionosphere disturbances · AGW · Troposphere–ionosphere coupling effect

## 1 Introduction

Solar activity and geomagnetic conditions play an important role in electron density variation of the ionosphere. The influences from the lower atmosphere also in some extent contribute to ionosphere variability. Several studies show that there is a close correlation between ionospheric wave-like disturbances and severe weather activities, such as thunderstorms, typhoon, tornadoes, hurricanes, and cold fronts (Kazimirovsky et al. 2003; Rishbeth 2006; Laštovička 2006). The influence altitudes are believed to reach the F<sub>2</sub> region, while the influence distances are over 1200–1800 km in some cases. Liu et al. (2006) found that during the 2004 Indian Ocean tsunami, the tsunami wave triggered atmospheric disturbances near the sea surface that traveled upward into ionosphere and significantly disturbed the ionosphere electron density. The horizontal speed is about 190 m/s in the ionosphere. Xiao et al. (2007) found that when typhoon toward ending, especially during a non-sunrise time, there are always sunrise-like phenomena. Nishioka et al. (2013) detected clear concentric waves and short-period oscillations caused by supercell-induced atmospheric gravity waves and acoustic resonances, respectively, after the 2013 Moore EF5 tornado. Otsuka et al. (2013) studied the medium-scale traveling ionospheric disturbances (MSTIDs) over Europe and found that the daytime and nighttime MSTID frequently occur in winter with southwestward propagation and winter/summer with southwestward propagation, respectively. The occurrence rate of both daytime and nighttime MSTIDs is higher at lower latitudes than at higher latitudes. Hernández-Pajares et al. (2006) found that daytime and nighttime MSTIDs are always related to the solar termi-

✉ Yibin Yao  
 ybyao@whu.edu.cn

<sup>1</sup> Chinese Antarctic Center of Surveying and Mapping, Wuhan University, Wuhan, China

<sup>2</sup> School of Geodesy and Geomatics, Wuhan University, Wuhan, China

<sup>3</sup> Department of Geomatics, National Cheng-Kung University, Tainan, Taiwan

nator and modulated by the solar cycle, the equatorward (from  $\sim 100$  to  $400$  m/s) and westward (from  $\sim 50$  to  $200$  m/s) horizontal propagation velocities are also presented, respectively. Komjathy et al. (2013) found that a real-time global TEC monitoring network is able to detect the acoustic and gravity waves generated by the earthquake and tsunami. Zhou et al. (2012) also reported the TIDs generated from thermospheric body forces created from the dissipation of primary gravity waves from deep tropospheric convection. The previous studies failed to demonstrate the definite connection between ionospheric disturbances and severe weather activities. In this study, based on the advantage of GNSS ionosphere monitoring, the ionosphere response process is given out in details and the results clearly show the strong spatial and time correlation between typhoon evolution and the ionosphere disturbances. The physical mechanism driving this correlation is also discussed in this paper.

The clear ionosphere disturbances responding to the typhoon were reported by several scholars, and the disturbances are characterized by periods in the range of 2–5 min (Baker and Davies 1969), 10–20 min (Hung et al. 1978; Huang et al. 1985; Liu et al. 2006), and over 30 min (Hung et al. 1978; Šauli and Boška 2001). Possible physical mechanisms have also been discussed, such as the increase in Turbopause (Mao et al. 2010), the ground electric field (Isaev et al. 2002; Sorokin et al. 2005), and the propagation of AGWs (Hung et al. 1978; Liu et al. 2006; Šindelářová et al. 2009).

On September 15, 2015 (Day of Year (DOY) 258), a low pressure area was generated on northwest of Guam over the Pacific. On September 23 (DOY266), the tropical cyclone was upgraded to a tropical storm and named Dujuan. When the typhoon passed through the Yaeyama Islands and Yonaguni, the measured wind speed was  $54.1$  m/s. On September 28 (DOY271), the typhoon landed on Taiwan, with wind speeds over  $58$  m/s, and after landfall, the typhoon structure was destroyed by the Central Mountains. Severe convective weather was formed during the typhoon path. On September 29 (DOY272), Dujuan travelled through Taiwan and into the Taiwan Strait. In this study, the period of interest is when Dujuan passed over the Taiwan. Due to the drag effect from the Central Mountains, the communication between the troposphere and ionosphere was captured with GNSS observations. The ionosphere's response to the severe convective weather in the troposphere is studied, and the disturbances of morphological characteristics are demonstrated. The possible physical mechanism is also provided.

## 2 Data and methodology

The data used in this study are the GNSS observations from Crustal Movement Observation Network of China

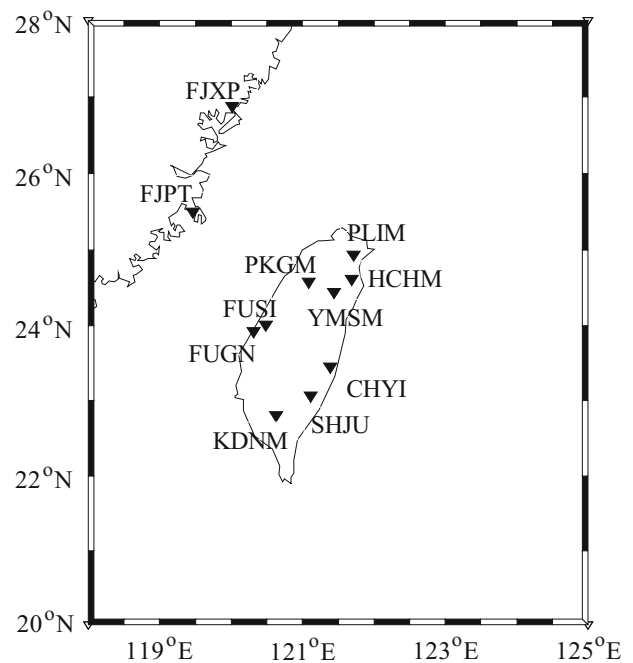


Fig. 1 Distribution of the GNSS stations

(CMONOC) and the Taiwan GNSS Tracking Network from National Land Surveying and Mapping Center in Taiwan. Figure 1 represents the distribution of the GNSS stations.

The influence of the intensity of the geomagnetic condition and the solar radiation on the ionosphere could be reflected in three indexes, Dst index, Kp index, and F10.7 index. Figure 2 demonstrates the variation in the three indexes covering from DOY256 to DOY273 of 2015. Figure 2 shows that there is a medium geomagnetic storm on DOY263, with  $Dst < -70$  nT, and  $Kp > 7$ . Except for DOY263, the geomagnetic conditions are quiet. Especially on DOY271 and DOY272,  $Dst > -15$  nT, and  $Kp < 4$  (On DOY271,  $Kp < 3$ ). According to the F10.7 index variation, the solar radiation is in steady state, within 0.4 and 4.0% of its mean value (from DOY268 to DOY274) on DOY271 and DOY272, respectively.

The details of the TEC derivation from the GNSS dual-frequency observations will not be discussed here (Liu et al. 2005). Processing of TEC sequence with a second-order operator is an effective method for ionosphere disturbance detection. The principle is to predict the current epoch's normal ionospheric changes using the prior two epochs' TEC variation. After removing the normal ionosphere changes from the current epoch, the abnormal changes can be precisely detected. Here, we have a set of Satellite-Station TEC (ssTEC) time sequences,

$$TEC_1, \dots, TEC_{i-1}, TEC_i, TEC_{i+1}, \dots, TEC_n \quad (1)$$

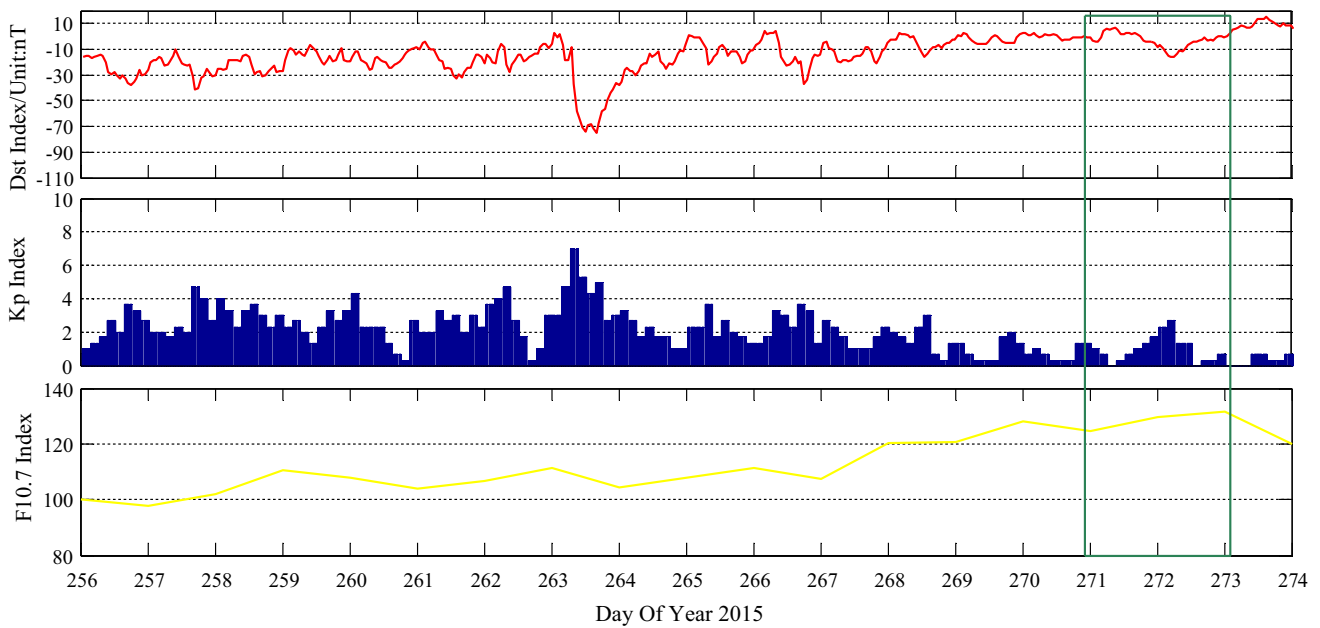


Fig. 2 Dst, Kp, and F10.7 indexes covering from DOY256 to DOY273 of 2015

The ionospheric disturbance at the  $i$ th epoch can be determined using the test value given by Eq. (2),

$$\begin{aligned}
 \text{TECV}_{\text{EST}} &= \text{TEC}_{i-1} - \text{TEC}_{i-2} \\
 &= \frac{f_1^2 f_2^2}{40.3 (f_2^2 - f_1^2)} [\Delta L_1(i-1) - \Delta L_2(i-1)] \\
 \text{TEC}_{\text{TEST}} &= \text{TECT} = \text{TEC}_i - (\text{TEC}_{i-1} + \text{TECV}_{\text{EST}}) \\
 \text{Then} \\
 \text{TECT} &= \frac{f_1^2 f_2^2}{40.3 (f_2^2 - f_1^2)} [(\Delta L_1(i) - \Delta L_2(i)) \\
 &\quad - (\Delta L_1(i-1) - \Delta L_2(i-1))] \\
 \Delta L_j(i) &= L_j(i) - L_j(i-1), j = 1, 2
 \end{aligned} \tag{2}$$

where  $L_1$  and  $L_2$  denote the carrier phases of the two frequencies  $f_1$  and  $f_2$ . TECT can be estimated in great accuracy using Eq. (2), so the anomaly value of the TEC sequence was easily confirmed. Combined with the Ionosphere Piece Point (IPP) coordinates of the TEC sequence, this detection method provides the disturbances' arrival time and location for each observation arc.

The accuracy of the carrier phase observations is hundreds of times higher than the pseudo-range observations. In Eq. (2), the ambiguity is removed by making the difference between neighboring epochs if no cycle slips occur. By using Eq. (2), the ssTEC variation between epochs is estimated. As shown in Eq. (3),

$$\text{TECV}_{\text{EST}} = \frac{f_1^2 f_2^2}{40.3 (f_2^2 - f_1^2)} [\Delta L_1 - \Delta L_2] \tag{3}$$

And the estimation precision of between epochs is obtained using Eq. (4),

$$\begin{aligned}
 \sigma_{\text{TECV}_{\text{EST}}}^2 &= \left[ \frac{f_1^2 f_2^2}{40.3 (f_2^2 - f_1^2)} \right]^2 [\sigma_{\Delta L_1}^2 + \sigma_{\Delta L_2}^2], \\
 \frac{f_1^2 f_2^2}{40.3 (f_2^2 - f_1^2)} &= -9.5196 \\
 \sigma_{L1} &= \lambda_1/100 + 0.0019 \text{ m}; \sigma_{L2} = \lambda_2/100 \\
 &= 0.0024 \text{ m} \\
 \sigma_{\text{TECV}_{\text{EST}}}^2 &= (-9.5196)^2 (0.0019^2 + 0.0024^2) \\
 \sigma_{\text{TECV}_{\text{EST}}} &= 0.03(\text{TECU})
 \end{aligned} \tag{4}$$

where  $\lambda_1$  and  $\lambda_2$  denote the wavelength of the two carrier phases  $L_1$  and  $L_2$ .

Using Eq. (4), the accuracy is approximately 0.03TECU. The elevation angle in the algorithm is  $40^\circ$ , so there is rarely multipath effect error in observation.

### 3 Results and analysis

#### 3.1 GNSS ssTEC sequences

Figure 3 demonstrates the ssTEC sequences of Sat.25 observed from two GNSS stations of the CMONOC and nine GNSS stations of the Taiwan GNSS network. The sequences were calculated using Eq. (3). After UTC13:00, there are clear disturbances in the ssTEC sequences (Fig. 3). In this figure, the black dots are used to mark the first arrival time of

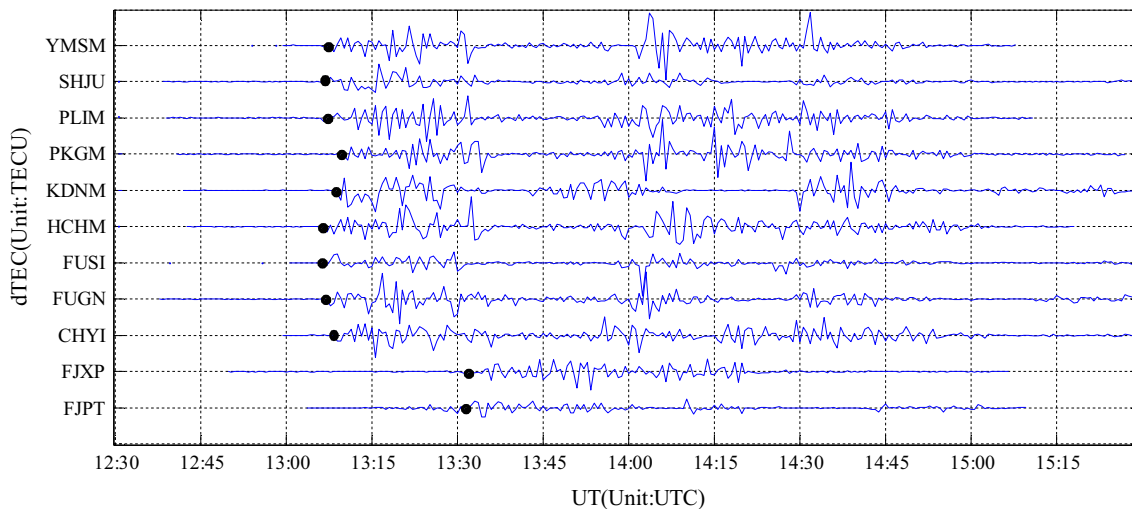


**Fig. 3** ssTEC sequences of Sat.25 observed from different GNSS stations on DOY271 (each y grid denotes 5TECU)

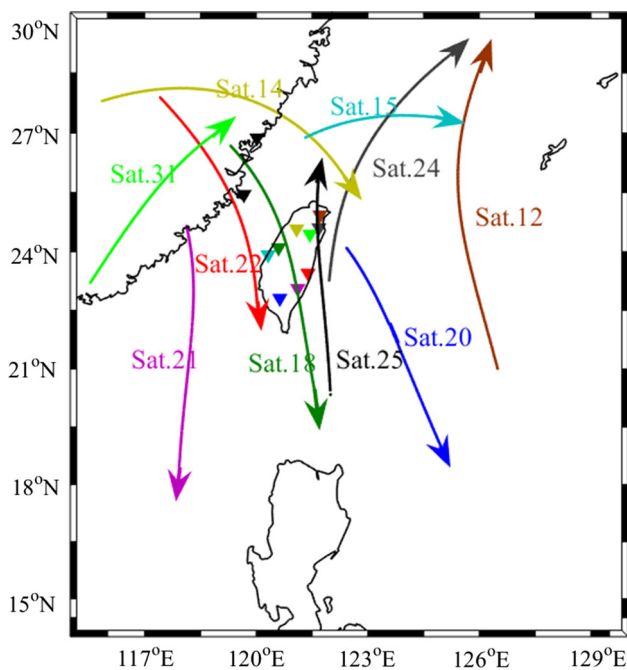


**Fig. 4** location and orientation of some IPP trajectories over Taiwan

the disturbances. Figure 4 shows the location and orientation of IPP trajectories over Taiwan (the IPP trajectories and orientation of all the 11 satellites corresponding to each station are calculated; due to limited space, Fig. 4 only lists one IPP trajectory of each station for simplification). The distribution of the GNSS stations (▼) in Fig. 4 is shown with different colors, and each station is corresponding to only one IPP trajectory, which has the same color (e.g., Station CHYI with red color corresponding to the Sat.22, Station KDNM with blue color corresponding to the Sat.20).

Further the disturbance is a special event coinciding with the typhoon landing. Figure 5 gives the ssTEC sequences of

Sat.12 observed for Station GHYI and Sat.21 observed for Station FUGN under the same period of 4 days surrounding the typhoon landing day. From this figure, it could be demonstrated that only on DOY271 (landing day) the clear ionosphere disturbances can be distinguished; the dramatic disturbances disappeared on the other days. Especially for one day after (DOY272) and two days before (DOY269) the typhoon landing, the ssTEC sequences varied smoothly which is in agreement with the accuracy estimated using Eq. (4). If there is no disturbance, the accuracy could be within 0.03TECU. The slight disturbances, which will be further discussed in Sect. 4, are shown in the sequences on DOY269 and DOY270 (Fig. 5).

Initially, the ionosphere disturbances were related to the typhoon landing (Figs. 2, 3). Taking advantage of multi-point monitoring and all-weather monitoring of GNSS technology, a deeper connection was determined.

The AGWs would propagate, at least initially, in all directions from the source (Vadas and Fritts 2004). Figure 6 shows a schematic diagram demonstrating the use of ssTEC to calculate the TID propagation velocity. The black point in Fig. 6 represents the assumed origin point on the ionosphere height of the Single Layer Model (SLM). The disturbances then spread to the surrounding area while several ssTEC sequences were passing through the area of interest. The different ssTEC sequences were treated as a space monitor for the TID, and they could catch the disturbances' propagation. For instance, if the IPP's coordinates and the disturbance arrival time are  $(X_1, Y_1), T_1$  and  $(X_2, Y_2), T_2$  at point 1 and point 2, respectively, then the estimation of propagation velocity could be calculated with Eq. (5).

$$V_h = \frac{\text{Dist}[(X_1, Y_1), (X_2, Y_2)]}{T_2 - T_1} \quad (5)$$

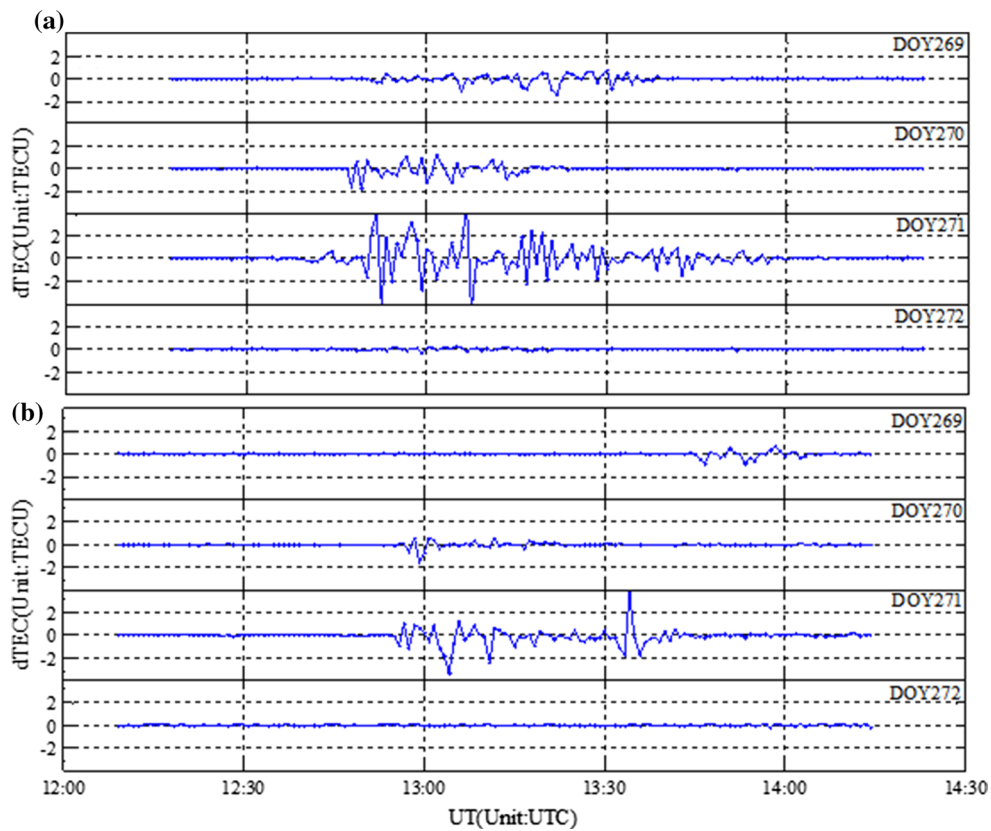


Fig. 5 ssTEC sequences of a Sat.12 for Station GHYI and b Sat.21 for Station FUGN

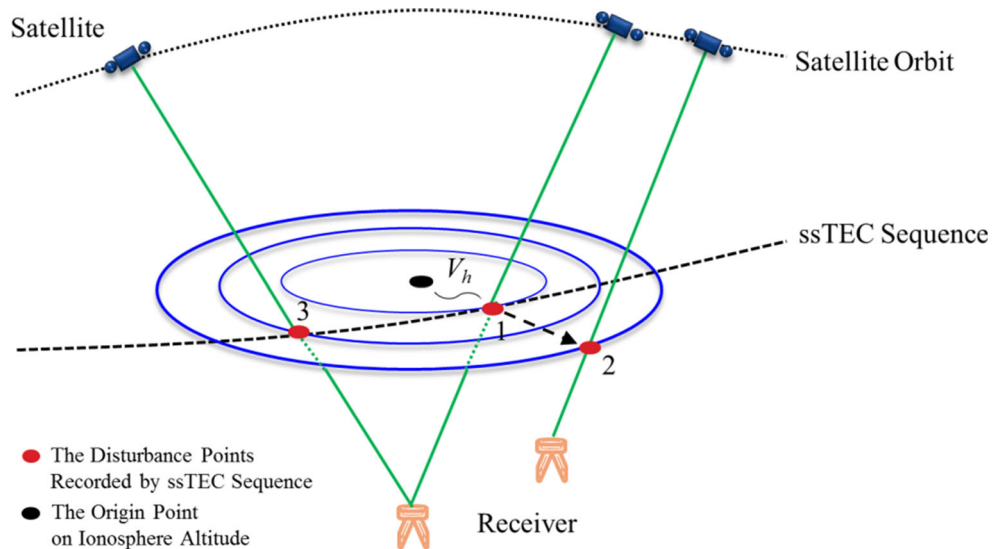


Fig. 6 Schematic diagram demonstrating the use of ssTEC to estimate the horizontal velocity of the ionosphere disturbance

Dist is the distance between two points. Each pair of disturbance points could be used to calculate the one group of propagation velocities.

In Fig. 7, only the horizontal propagation velocity on the SLM height is considered. The effect of traveling time from the origin point on a terrestrial surface to the ionosphere's

altitude is ignored. The vertical traveling velocity will be discussed in Sect. 3.2. The average value of the horizontal propagation velocities is approximately 240 m/s, which will be used in the two-dimensional searches for the origin point on the Earth's surface.

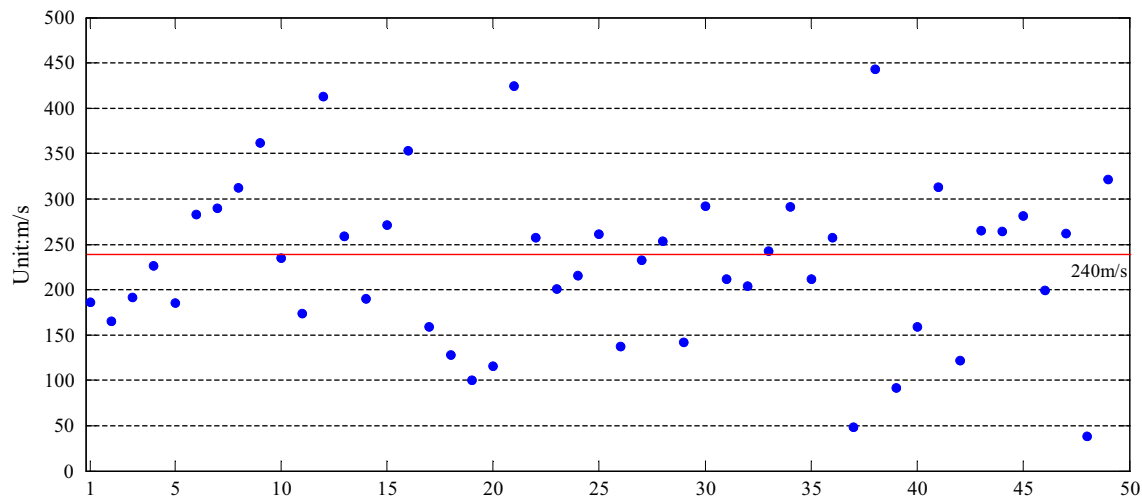


Fig. 7 Estimation of the horizontal velocity using different pairs of disturbance points

### 3.2 The grids search for the trigger source area

Multi-point measurements will help to determine of the origin of the waves (Šindelářová et al. 2009). GNSS TEC monitoring meets the requirements of multi-points observations, so the two global grids search method (Lee and Lahr 1972; Liu et al. 2010) is implied to determine the TID origin on the Earth's surface. Initially, the possible trigger area covering from 14°N to 30°N and from 115°E to 130°E was divided into two-dimensional grids, with a resolution of 1° in longitude and latitude. With the propagation velocity estimated in Sect. 3, the traveling time residuals could be calculated using Eq. (7).

According to the linear theory for a dispersion relation of AGWs in an isothermal atmosphere, the main regulars for AGWs propagation are as follows (Hines 1960; Xiao et al. 2007),

1. When AGWs propagate upwards, the amplitude enhances gradually so as to satisfy the requirements of energy conservation. During the wave upward propagation, the wave is actually strongly amplified by the coupled effect of the conservation of kinetic energy  $E_k = \frac{1}{2}\rho v^2$ , and the exponential decrease in the air's density  $\rho$  (Occhipinti 2015).
2. Group velocity is gradually enhanced along with the increasing frequency, and the direction of the energy flux tends to become horizontal as the frequency decreases.
3. The vertical component of AGWs phase velocity is opposite of that of the group velocity.

In this study, a possible path for the disturbance propagation is required to be given in advance and is shown in Fig. 8. Here, two different paths are applied, which provide an upper and lower limit of the traveling distance, respectively. The

maximum traveling distance is that disturbances are traveling from the origin point vertically up to ionosphere altitude and then horizontally to the IPPs, and the minimum traveling distance is that the disturbances are traveling from the origin point radially into the ionosphere. Under the first case, the boundary conditions are set in advance as shown in Eq. (6),

$$(X_0, Y_0), V_v, V_h, T_D \tag{6}$$

where  $(X_0, Y_0)$  are the grids' coordinate,  $V_v$  and  $V_h$  are the vertical velocity and the horizontal velocity, respectively, as shown in Fig. 8.  $V_h = 240$  and  $V_v = 50$  m/s are applied here (the vertical velocity value was taken from Artru et al. 2005).  $T_D$  is the disturbance arrival time, as marked with black dots in Fig. 3.

The time residuals are calculated using Eq. (7).

$$\begin{aligned} T_v &= \frac{H_I}{V_v}, T_h = \frac{dist[(X_i, Y_i), (X_0, Y_0)]}{V_h} \\ T_E &= T_0 + T_v + T_h \\ V &= T_E - T_D \end{aligned} \tag{7}$$

where  $H_I$  is the ionosphere altitude (450 km).  $T_v$  is the traveling time from the disturbance origin to the ionosphere altitude.  $T_h$  is the traveling time from the Point 1 in Fig. 8 to IPPs.  $T_0$  is the typhoon landing time at Taiwan.  $T_E$  is the estimated disturbance arrival time.  $V$  is the time residual between the estimated and real disturbance time.

Under the second case, the time residuals are calculated using Eq. (8).

$$\begin{aligned} V_{Ri} &= \frac{distR[(X_i, Y_i), (X'_0, Y'_0)]}{T_i - T_0} \\ T_E &= \frac{distR[(X_i, Y_i), (X'_0, Y'_0)]}{V_R} \end{aligned}$$

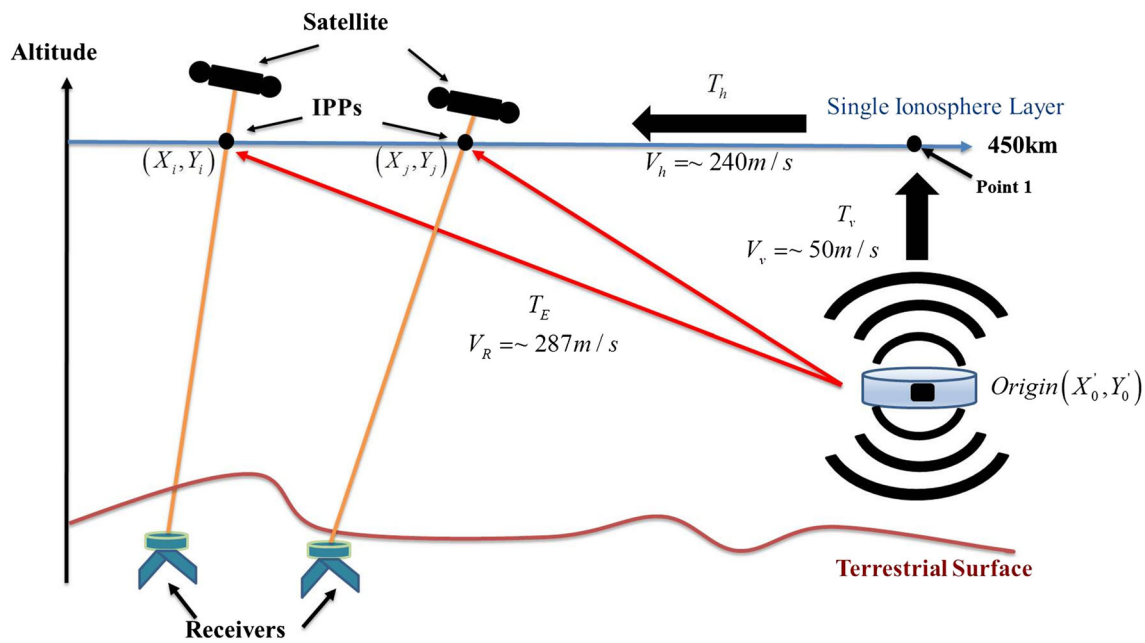


Fig. 8 Schematic diagram demonstrating the use of ground-based GPS receivers to determine the TID origin

$$V = T_E - T_D \tag{8}$$

where  $distR$  is the straight line distance between grids' coordinate on the ground with the IPPs which are the first arrival time of the disturbances.  $(X'_0, Y'_0)$  are the grids' coordinate on the ground.  $T_i$  are the first disturbances arrival time of IPPs.  $V_R$  is the average value of  $V_{Ri}$  ( $i = 1, 2, 3 \dots$ ).

When typhoon landing at  $T_0$ , the triggered AGWs radially propagate into the ionosphere and cause the ionospheric disturbances. Once the first disturbances onset time ( $T_i$ ) of all ssTEC sequences is recorded, the radial velocity from each grid on the ground to all IPPs could be calculated using Eq. (8). The average value with minimum standard deviation is the criterion of the final radial velocity. Similarly, when the standard deviation yields the minimum, the radial velocity is determined.

Table 1 illustrates 8 possible radial velocities of AGWs, we select the set of values with the smallest standard deviation, so we determine the radial propagation velocity is  $\sim 287$  m/s in this case.

Figure 9a, c shows the distribution of the time residuals estimated with the disturbance information (IPP coordinate and disturbance time) recorded by the ssTEC sequence propagating ways (vertically then horizontally and radially), respectively. As expected, the time residuals appear as the concentric circles, and the minimum residual circle passes through Taiwan. The TID origin point could be defined as the cross-point of the different minimum residual circles. Figure 9b, d shows the residuals distribution estimated from

Table 1 Eight possible radial velocities of AGW

	Latitude <sup>a</sup>	Longitude <sup>a</sup>	$V_R^b$ (m/s)	Std ( $V_R$ )
1	24	121	$\sim 274$	26.49
2	22	119	$\sim 265$	42.36
3	23	120	$\sim 267$	33.88
4	26	120	$\sim 332$	31.13
5	23	121	$\sim 253$	27.31
6	<b>25</b>	<b>122</b>	<b><math>\sim 287</math></b>	<b>25.76</b>
7	25	123	$\sim 279$	27.40
8	26	123	$\sim 305$	29.54

<sup>a</sup> The latitude and longitude of each grid on the ground

<sup>b</sup> The average value of calculated velocities from each grid on the ground to all first disturbance IPPs on the ionosphere height

over 10 ssTEC sequences, and it could be seen that the most possible area for the TID origin is in Taiwan, meaning that the ionosphere disturbance is likely related to the typhoon landing.

### 3.3 Other data

The ionosonde data observed by Xiamen station are used to validate this ionosphere disturbance. The ionospheric parameters foF2 daily variations from DOY269 to DOY272 are shown in Fig. 10. The foF2 could be converted to electron density using Eq. (9).

$$f[\text{Hz}] = 8.98\sqrt{Ne}(\text{m}^{-3}) \tag{9}$$

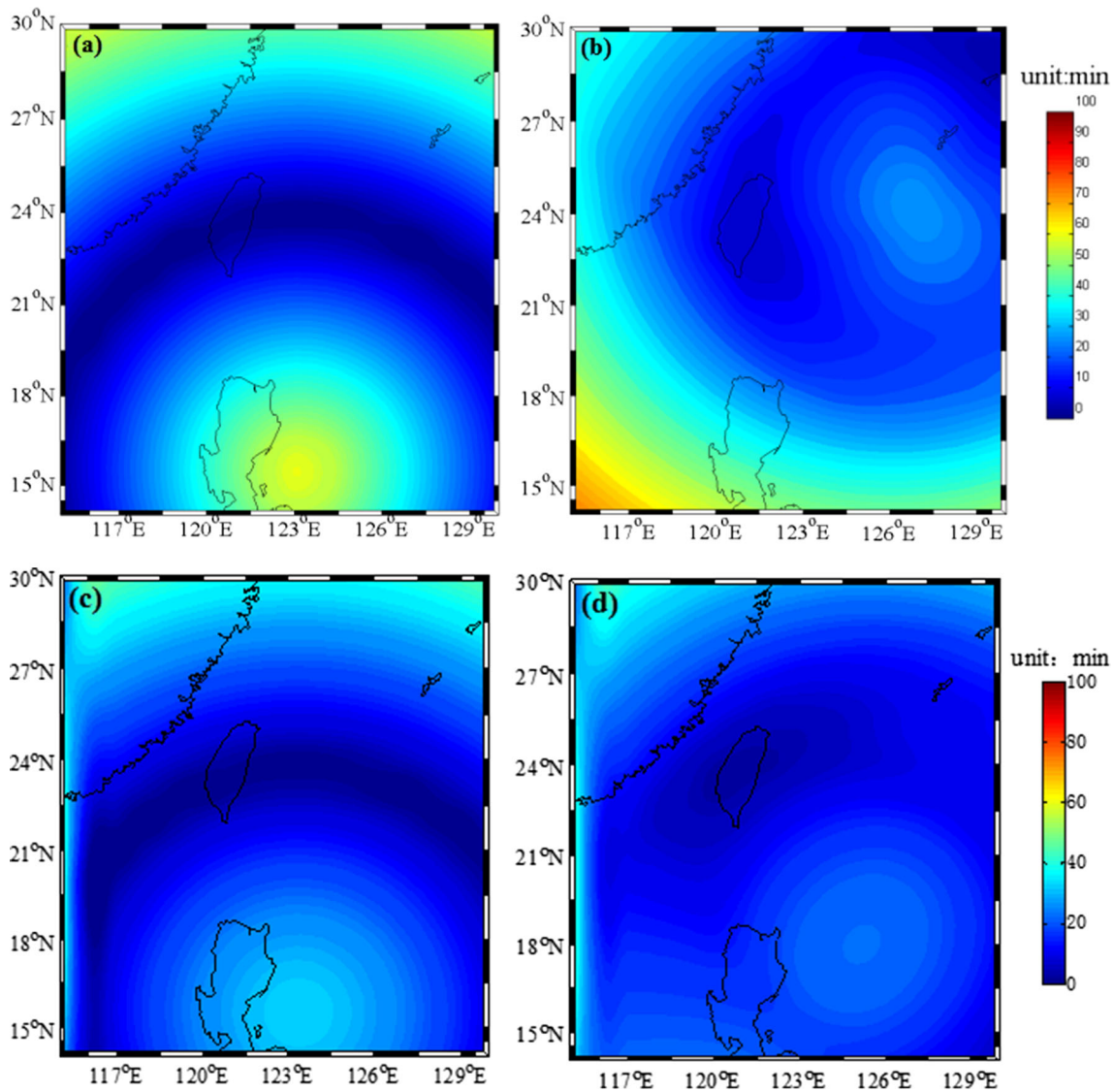


**Fig. 9** Time residual distribution based on the two-dimensional grids search method. **a, c** The results using one disturbance point in two possible propagating ways. **b, d** The results using a group of disturbance points in two possible propagating ways

The foF2 variations under quiet period (from DOY266 to DOY270 and from DOY272 to DOY273) are shown as gray bands and their widths correspond to  $\pm 1$  standard deviation. The background values could be calculated according to Eq. (10).

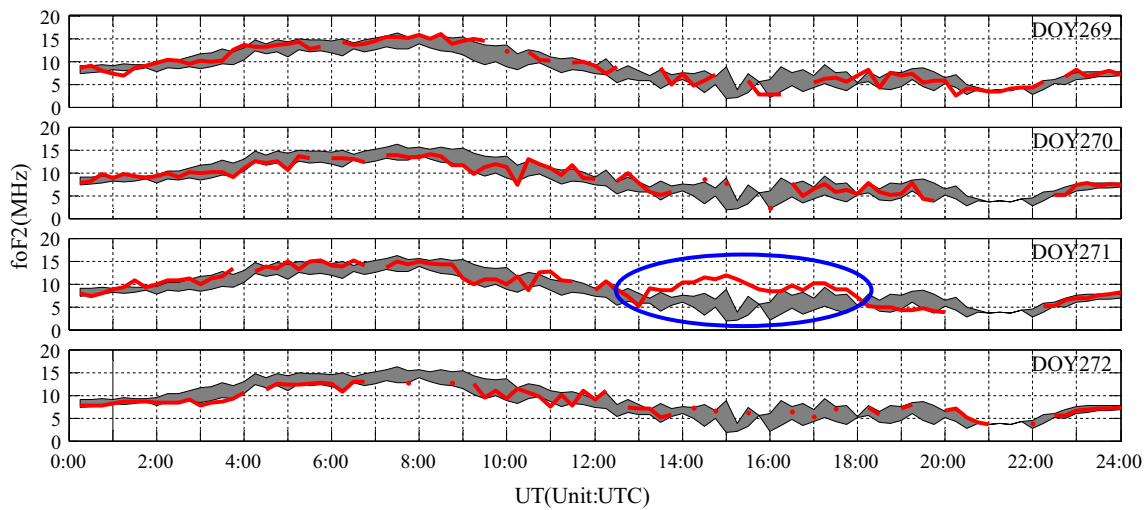
$$\begin{aligned}
 &foF2_1 foF2_2 \dots foF2_{n-1} \\
 aver &= average(foF2_1 foF2_2 \dots foF2_{n-1}) \\
 std &= stdev(foF2_1 foF2_2 \dots foF2_{n-1}) \\
 upper &= aver + 1 \times std \\
 lower &= aver - 1 \times std
 \end{aligned}
 \tag{10}$$

Figure 10 shows that there were significant positive anomalies after UTC13:00 in DOY271 as the foF2 values suddenly increased to  $\sim 10$  MHz and decreased to normal

values about five hours later. The abnormal onset time of the GNSS observations is also around UTC13:00, which is consistent with the result in Figs. 3 and 5. Thus, the ionosphere disturbances can be detected by both ssTEC sequences and foF2 values after typhoon landing. It is also worth noting that there are no obvious disturbances on the day after (DOY272) and two days before (DOY269) typhoon landing using the ionosonde data.

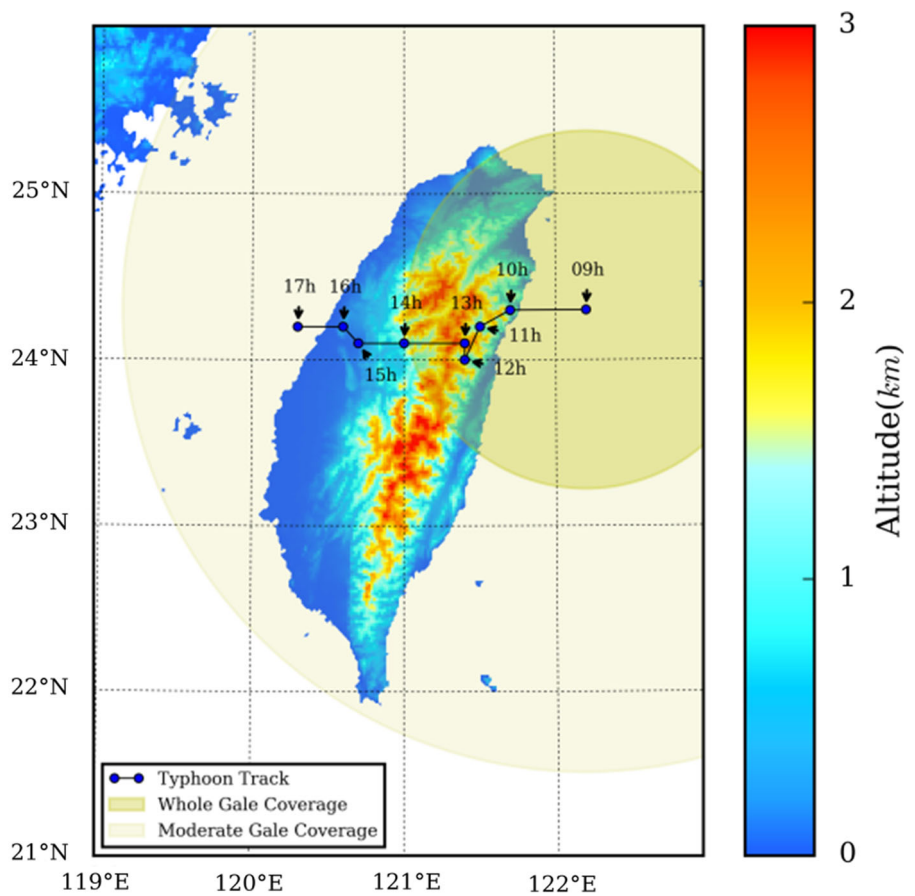
#### 4 Discussion and conclusion

Waves with periods longer than the Brunt–Vaisala periods are termed as gravity waves, which can be triggered by a number of sources including meteorological activity, auroral activity,



**Fig. 10** Variations of the ionospheric parameter foF2 obtained at Xiamen from DOY269 to DOY272 (red lines). The gray bands are  $\pm 1$  standard deviation of quite day values

**Fig. 11** Topographic map of Taiwan with the footprint of Dujuan Typhoon [the figure is plotted by matplotlib (<http://matplotlib.org>), and the elevation data are from etop1 (<https://www.ngdc.noaa.gov/mgg/global/global.html>)]



earthquakes, and eruptions (Laštovička 2006; Šindelářová et al. 2009). Ionosphere disturbances usually happen when typhoon is near the coast or landing because the rapid loss of momentum and viscous interactions could be a factor in exciting AGWs with various frequencies (Xiao et al. 2007). AGWs would influence very high atmospheric altitudes because of their relatively large vertical wavelengths. Zones of deep

tropical convection are the dominant sources of convectively generated gravity waves and possibly the most important source of high frequency gravity waves on Earth (Vadas and Fritts 2004). Here, the ionosphere disturbance responding to Dujuan Typhoon could be interpreted by the AGWs. Terrain is one of the main influencing factors for AGW generation. Brooks et al. (2003) noted that the high terrain of the Rocky

Mountains generates steep lapse rates in the plains of the USA. Figure 11 shows the topographic map of Taiwan and the time-labeled typhoon footprint. From the east coast to west coast of Taiwan, there are five main mountain ranges: the Coast Mountains, the Central Mountains, the Snow-Capped Mountains, the Yushan Mountains, and the Alishan Mountains. When the typhoon passes through a mountainous area, the low air pressure allows the severe convective weather to form. At this point, the AGWs are more easily generated on the leeward side of the mountains. At the same time, with the impact of the dramatic undulating terrain, the AGWs can propagate to the ionosphere altitude and disturb the ionosphere electron density. Before the typhoon's landfall, the whole gale coverage already influenced the mountain areas (Fig. 11), which allowed the ionosphere disturbances to be observed one day before the landing day, while the disturbances disappeared one day after the landing day.

In this study, the ionosphere disturbances response to 2015 Dujuan Typhoon were discussed. The ionosphere disturbances were clearly shown using the ssTEC sequences after removing the de-trended TEC variation. By comparing the ssTEC sequences before and after the typhoon landing day, a relationship between the ionosphere disturbances and the typhoon was reconfirmed, as there are no obvious disturbances on other days. The foF2 data also show clear anomalies which is consistent with the GNSS analysis.

Furtherly, based on the linear theory for a dispersion relation of AGWs, the disturbances propagation velocity in the ionosphere was estimated using multi-point observations. The average horizontal velocity and radial velocity are approximately 240 and 287 m/s, respectively. Using the two-dimensional grid search method, we found the origin of the disturbance on the Earth's surface. The origin is set at the west coast of Taiwan.

Finally, a possible physical mechanism is discussed in this study. The TID is triggered by the propagation of AGWs. When the typhoon lands, the latent heat input from the sea surface is rapidly reduced; at the same time, low pressure brought severe convective weather. Due to the drag effects from the mountains located in western Taiwan, a high lapse rate in the air creates an ideal location for development of AGWs. Two possible disturbances traveling paths provide an upper and lower limit of the distance, respectively. As indicated by Vadas and Fritts (2009), the AGWs would not be able to propagate freely because of wave breaking, critical level absorption, and reflection in the stratosphere. The deep coupling effect still requires further study.

**Acknowledgements** We acknowledge the CMONOC for providing the GPS data via the GNSS Center at Wuhan University, the National Land Surveying and Mapping Center for providing the Taiwan GNSS Network data, the IGS for providing the orbit data. We also thank the NASA for providing magnetic index data, the ACE Science Center for providing solar wind data. This research was financially supported

by the National Natural Fund of China (41274022, 41231064, and 41574028) and the Fundamental Research Funds for the Central Universities (2042016kf0037). Special thanks to Dr. Chen Zhou in School of Electronic Information, Wuhan University, for discussing the physical mechanism of AGWs propagation. We also appreciate Dr. Jing Liu of Institute of Earthquake Science, China Earthquake Administration and Dr. Yungang Wang of National Center for Space Weather, China Meteorological Administration for providing the ionosonde data.

## References

- Artru J et al (2005) Ionospheric detection of gravity waves induced by tsunamis. *Geophys J Int* 160(3):840–848
- Baker DM, Davies K (1969) F2-region acoustic waves from severe weather. *J Atmos Terr Phys* 31:1345–1352
- Brooks HE, Lee JW, Craven JP (2003) The spatial distribution of severe thunderstorm and tornado environments from global reanalysis data. *Atmos Res* 67–68:73–94
- Hernández-Pajares M, Juan JM, Sanz J (2006) Medium-scale traveling ionospheric disturbances affecting GPS measurements: spatial and temporal analysis. *J Geophys Res Space Phys* 111(A7):A07S11
- Hernández-Pajares M, Juan JM, Sanz J, Aragón-àngel A (2012) Propagation of medium scale traveling ionospheric disturbances at different latitudes and solar cycle conditions. *Radio Sci* 47(6)
- Hines CO (1960) Internal atmospheric gravity waves at ionospheric heights. *Can J Phys* 38:1441–1481
- Huang YN, Cheng K, Chen SW (1985) On the detection of acoustic-gravity waves generated by typhoon by use of real time HF Doppler frequency shift sounding system. *Radio Sci* 20:897–906
- Hung RJ, Phan T, Smith RE (1978) Observation of gravity waves during the extreme tornado outbreak of 3 April, 1974. *J Atmos Terr Phys* 40:831–843
- Isaev NV, Sorokin VM, Chmyrev VM, Serebryakova ON, Yashchenko AK (2002) Disturbance of the electric field in the ionosphere by sea storms and typhoons. *Cosmic Res* 40(6):591–597
- Kazimirovsky ES, Herraiz M, De la Morena BA (2003) Effects on the ionosphere due to phenomena below it. *Surv Geophys* 24:139–184
- Komjathy A, Galvan DA, Stephens P, Butala MD, Akopian V, Wilson B, Verkhoglyadova O, Mannucci AJ, Hickey M (2013) Detecting ionospheric TEC perturbations caused by natural hazards using a global network of GPS receivers: the Tohoku case study. *Earth Planets Space* 64(12):1287–1294. doi:10.5047/eps.2012.08.003
- Laštovička J (2006) Forcing of the ionosphere by waves from below. *J Atmos Sol-Terr Phys* 68:479–497
- Lee WHK, Lahr JC (1972) HYPO71: A computer program for determining hypocenter, magnitude, and first motion pattern of local earthquakes (No. 72–224). US Geological Survey
- Liu ZZ, Gao Y, Skone S (2005) A study of smoothed TEC precision inferred from GPS measurements. *Earth Planets Space* 57(11):999–1007
- Liu JY et al (2006) Ionospheric GPS total electron content (TEC) disturbances triggered by the 26 December 2004 Indian Ocean tsunami. *J Geophys Res* 111:A05303
- Liu JY et al (2010) Coseismic ionospheric disturbances triggered by the Chi-Chi earthquake. *J Geophys Res* 115:A08303
- Mao T et al (2010) Effects of typhoon Matsa on ionospheric TEC. *Chin Sci Bull* 55:712–717
- Michi N, Tsugawa T, Kubota M, Ishii M (2013) Concentric waves and short-period oscillations observed in the ionosphere after the 2013 Moore EF5 tornado. *Geophys Res Lett* 40(21):5581–5586. doi:10.1002/2013GL057963
- Occhipinti G (2015) The seismology of the planet Mongo: the 2015 ionospheric seismology review. In: Morra G, Yuen DA, King S,

- Lee SM, Stein S (eds) Subduction dynamics: from mantle to mega disasters. AGU Books. ISBN: 978-1-118-88885-8
- Otsuka Y, Suzuki K, Nakagawa S, Nishioka M, Shiokawa K, Tsugawa T (2013) GPS observations of medium-scale traveling ionospheric disturbances over Europe. *Ann Geophys* 31(2):163–172. doi:[10.5194/angeo-31-163-2013-supplement](https://doi.org/10.5194/angeo-31-163-2013-supplement)
- Rishbeth H (2006) F-region links with the lower atmosphere? *J Atmos Sol-Terr Phys* 68:469–478
- Šauli P, Boška J (2001) Tropospheric events and possible related gravity wave activity effects on the ionosphere. *J Atmos Sol-Terr Phys* 63:945–950
- Šindelářová T, Burešová D, Chum J, Hruška F (2009) Doppler observations of infrasonic waves of meteorological origin at ionospheric heights. *Adv Space Res* 43:1644–1651
- Sorokin VM et al (2005) Strong DC electric field formation in the low latitude ionosphere over typhoons. *J Atmos Sol Terr Phys* 67:1269–1279
- Vadas SL, Fritts DC (2004) Thermospheric responses to gravity waves arising from mesoscale convective complexes. *J Atmos Sol-Terr Phys* 66:781–804
- Vadas SL, Fritts DC (2009) Reconstruction of the gravity wave field from convective plumes via ray tracing. *Ann Geophys* 27:147–177
- Xiao Z, Xiao S, Hao Y, Zhang D (2007) Meteorological features of ionospheric response to typhoon. *J Geophys Res: Sp Phys* 112(A4)
- Zhou C, Zhao Z, Yang G, Chen G, Hu Y, Zhang Y (2012) Evidence of low-latitude daytime large-scale traveling ionospheric disturbances observed by high-frequency multistatic backscatter sounding system during a geomagnetically quiet period. *J Geophys Res* 117:A06302. doi:[10.1029/2012JA017605](https://doi.org/10.1029/2012JA017605)